






Whole anterior segment and retinal swept source OCT for comprehensive ocular screening

ANA RODRÍGUEZ-ARAMENDÍA,^{1,2,*}  FERNANDO DÍAZ-DOUTÓN,² 
JOSÉ FERNÁNDEZ-TRULLÀS,² POL FALGUERAS,² LAURA
GONZÁLEZ,¹ JAUME PUJOL,² IRENEUSZ GRULKOWSKI,³  AND
JOSÉ LUIS GÜELL¹

¹*Instituto de Microcirugía Ocular (IMO), Josep María Lladó 3, Barcelona 08035, Spain*

²*Center for Sensors, Instruments and Systems Development (CD6), Universitat Politècnica de Catalunya (UPC), Rambla Sant Nebridi 10, Terrassa 08222, Barcelona, Spain*

³*Institute of Physics, Faculty of Physics, Astronomy and Informatics, Nicolaus Copernicus University, ul. Grudziądzka 5, 87-100 Toruń, Poland*

*ana.rodriguez.aramendia@upc.edu

Abstract: Whole eye visualization and morphometry are of high relevance in clinical practice. However, most standard ophthalmic OCT instruments are dedicated either to retinal or to anterior segment imaging. We demonstrate a swept source optical coherence tomography system (SS-OCT) that images both the whole anterior segment and the retina alternately using a single source and detector. A pilot population was imaged with the proof of concept prototype. We demonstrate the clinical potential of whole eye OCT screening for the description and early detection of relevant clinical features in the anterior segment and retina of several patients.

© 2021 Optical Society of America under the terms of the [OSA Open Access Publishing Agreement](#)

1. Introduction

Optical coherence tomography (OCT) is a noninvasive technique that permits to generate cross-sectional and volumetric images of the human eye with micrometer resolution. Since its invention [1,2], the use of OCT instruments has been widely established in the daily ophthalmic practice, guiding clinicians in the diagnosis, follow-up, and treatment of ocular pathologies [3–8]. The handling of a number of eye diseases, such as glaucoma, cataract, ocular trauma, ocular tumors, etc., involves the observation of both the anterior segment and the retina and the determination of geometrical relations between ocular structures across the entire eye globe [9]. Most commercial OCT instruments are dedicated either to retinal or to anterior segment imaging, making the use of several instruments necessary. Currently, few commercial instruments can image both parts of the eye. For example, some OCTs dedicated to retinal imaging permit to image the anterior segment, but require adding optics or present limitations in field of view and/or imaging depth range. In this regard, an OCT instrument that could acquire three dimensional (3-D) representations covering the entire eye could be used instead of other imaging devices in the aforementioned clinical tasks.

However, imaging the anterior segment and the retina of the human eye with a wide field of view with the same OCT instrument poses important challenges. Firstly, OCT systems feature limited imaging depth ranges. For example, standard clinical OCT systems are typically restricted to 2–3 mm, while the full eye length of the human eye extends to approximately 24 mm. Secondly, due to the human eye optics and length in the anterior segment and the retina, it requires a considerably long depth of focus illumination. A conventional sample arm based on Gaussian optics would need a significantly loosely focused beam to achieve such a long depth of focus, and consequently, it would sacrifice lateral resolution. Finally, obtaining wide field of view images of both segments of the eye requires different scanning strategies due to the human eye's anatomy:

telecentric scanning for the anterior segment imaging and angular scanning of a collimated beam with its pivot close to the pupil plane of the eye for retinal imaging.

Several approaches have been proposed to overcome these barriers. The first reports in whole eye imaging consisted of spectral domain OCT (SD-OCT) systems that integrated two OCT subsystems combined by means of optical or mechanical switches in the reference and/or the sample arm, where some or many elements of the OCT engine (source, fiber interferometer, spectrometer, etc.) were duplicated. An early implementation of this solution required two OCT data sets to image the whole anterior segment, in between which the reference arm length was adapted, and a third change for retinal imaging, featuring a considerably limited field of view [10]. Other implementations permitted to image the retina with a wider field of view thanks to an adapted interface for retinal imaging in the sample arm, combined with the anterior segment one using two beam splitters or polarization multiplexing (two orthogonal polarization modes propagate through two dedicated interfaces for retinal and anterior segment imaging). In these works, either only the anterior chamber is imaged [11] or entire anterior segment visualization is achieved by employing off-pivot based complex conjugate removal [12] and full range complex (FRC) SD-OCT [13].

Whole eye imaging systems based on swept source OCT (SS-OCT) technology also appeared soon after. Advances in swept source technology enabled to achieve tens of millimeters imaging depth ranges, facilitating applications in which an enhanced depth range was required. The design of the SS-OCT system was crucial to keep the desired axial resolution while attempting to increase the depth range, since there may be a trade-off between these parameters. In this sense, an imaging platform based on a vertical cavity surface emitting laser (VCSEL) that overcame the coherence length limitation of imaging along the length of the human eye was demonstrated [14]. Measurements of the axial eye length were achieved by a loosely focused beam scanning the anterior segment with a telecentric configuration, which revealed a much reduced field of view of the retina with poor lateral resolution. In the quest for imaging along the axial length without sacrificing lateral resolution, the use of tunable optics in the sample arm of a SS-OCT system was proposed [15]. An electrically tunable lens changed power on a B-scan basis permitting to enhance the visualization of structures at different depths.

Another solution for the interferometric limitation of OCT systems proposed the use of successive coherence revival windows of short cavity lasers [16] and was used to image the anterior segment and retina without the need of adapting the reference arm [17]. Following works elaborating on the coherence revival implementation of whole eye imaging appeared, either featuring a compact sample arm that switches from an anterior segment interface to a retinal one using two mirrors [18] or exploiting polarization multiplexing [19]. These systems achieve retinal field of views of 22° and 55° , respectively. The wide field of view of the latter allows for retinal curvature measurements. However, both systems only image the anterior chamber, lacking visualization of the posterior end of the crystalline lens. A whole eye SS-OCT system powered by a long coherence length source and utilizing polarization multiplexing in the sample arm, permitted to image the whole anterior segment and the retina [20]. However, this implementation required duplicated interferometers and detection channels.

Exploiting further the comprehensive information that whole eye OCT platforms provide, some research applications proposed their use to evaluate dynamic aspects of the visual function, too [8]. A binocular anterior and posterior OCT platform [21] was used to perform pupilometry tests and assess strabismus [22]. However, the anterior segment modality of that system just visualized the anterior chamber of the eyes, which limited its use in the study of the crystalline lens.

In this work, we demonstrate a SS-OCT prototype that can image the whole anterior segment and the retina alternately utilizing a single source and a single detection channel. The proof of concept demonstration of the system features a simple sample arm fully constructed with

off-the-shelf optics and a fold mirror that allows switching from one modality to the other. Visualization of the whole anterior segment and the retina enables whole eye screening on a single instrument, which provides a comprehensive description of features of clinical relevance all over the ocular structures.

2. Methods

A custom whole eye OCT system was designed to meet the following general performance specifications:

- (a) The same instrument should image the anterior segment and the retina alternately. The separation of imaging modes will enable to address the specific requirements of both imaging modes.
- (b) The anterior segment modality should allow whole anterior segment imaging in a single OCT capture, from corneal apex to posterior face of the lens and from nasal to temporal iridocorneal angle. Therefore the field of view (FOV) should be at least $13 \text{ mm} \times 13 \text{ mm}$, the imaging depth range should at least be 13 mm in air (one has to account for refractive indexes of the ocular components) and the Rayleigh range should exceed 2 mm (to provide sufficient illumination and photon collection efficiency).
- (c) The retinal modality should image the macula and the optic disc, meaning that the retinal FOV should be about 24° , with a lateral resolution of at least $15 \text{ }\mu\text{m}$. High lateral resolution desired in retinal imaging mode should facilitate visualization of the retinal vasculature (including capillary network).
- (d) Axial resolution in both modalities should at least be $15 \text{ }\mu\text{m}$. The axial resolution determined by the light source bandwidth is more critical for retinal imaging due to the layer-like organization of retinal tissue. Therefore, this specification can be considered as a trade-off between detailed structures of the retina and the anterior segment of the eye.

From these general requirements, specifications for the OCT engine and the optical and optomechanical performance requirements of the sample arm were derived and addressed through combined optical and optoelectronic design, as detailed in the following subsections.

2.1. Whole anterior segment / retinal SS-OCT design

The SS-OCT instrument was based on an all-in-fiber interferometer (Fig. 1). The light source used in the prototype was a swept source engine (Axsun Technologies Inc., USA) with 50 kHz sweep rate and a central wavelength of 1050 nm. The spectrum of the source had a wavelength tuning range of about 110 nm and offered a 16 mm coherence length, which sufficed for whole anterior segment imaging in a single shot.

A 12 bit high speed (1 GS/s) digitizer (ATS9371, Alazar Technologies Inc., Canada) and a 1 GHz bandwidth AC coupled balanced InGaAs detector (PDB481C-AC, Thorlabs Inc., USA) composed the detection segment of the system (labelled in Fig. 1 as ADC and PDB, respectively). The source, detector and digitizer were chosen jointly to provide the axial image depth range needed for whole anterior segment imaging, keeping an axial resolution of about $10 \text{ }\mu\text{m}$, at the fastest sweep rate available, and so that imaging of the anterior segment and retina was possible [23]. An analog output card (PCIe-6738, National Instruments, USA) was utilized to generate the driving voltage signals that control a set of XY galvanometric mirrors (8320K, Cambridge Technology Inc., USA). The acquisition software was developed in LabView, permitting the synchronization of the sweeps with the start of the digitizer's acquisitions and the movement of the scanners. Real time display of OCT images was provided for fine alignment of the eye.

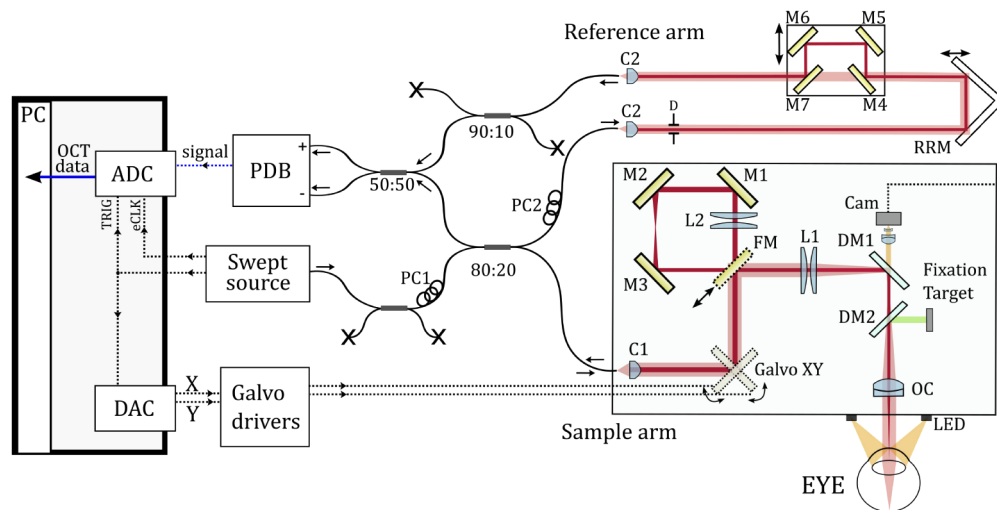


Fig. 1. The sample arm of the instrument is composed by different spectral channels. The red and pink paths are the OCT channels for anterior and posterior segment imaging, respectively. The orange path stands for the pupil imaging and the green path indicates the fixation channel. L1, L2 and OC: groups of lenses; C1, C2: fiber collimators; FM: fold mirror; M1-M7: mirrors; PC1, PC2: polarization controllers; RRM: retroreflection mirror; D: diaphragm; DM1, DM2: dichroic mirrors; ADC: analog-to-digital converter or digitizer; DAC: digital-to-analog card or analog output card; TRIG: signal indicating the start a sweep and eCLK: external clock signal for k-linear sample acquisition.

The all-in-fiber interferometer was composed of a series of 2×2 (2 inputs, 2 outputs) fiber couplers of different splitting ratios (AC Photonics Inc., CA, USA). The couplers were based on a HI-1060 optical fiber, a mode-field diameter of $6.2 \mu\text{m}$ at 1060 nm and a numerical aperture of 0.14. Two customized fiber polarization controllers (PC1 and PC2) were used to optimize the OCT signal, composed by 3 pads in such a way that they operated as quarter-half-quarter wave plate combinations, which allow for arbitrary transformations of the polarization state.

The reference arm of the system featured a single-pass configuration composed by two collimators (C2), input and output, and a gold retroreflection mirror (RRM) mounted on top of a 25 mm travel translation stage, with micrometer resolution for fine tuning of its length. An iris diaphragm (D) was used to control the reference arm light power. A group of mirrors (M4-M7) mounted on a translation stage allowed changing its length between both imaging modalities.

2.2. Design of the sample arm

The sample arm was composed by three spectrally separated channels, as illustrated in Fig. 1 with different colors. The OCT channels operated at a central wavelength of 1050 nm (red and pink paths), as described previously. A LED-based fixation target emitted in the visible range (green path). A ring of four LEDs (central emission at 850 nm) located around the objective lens (OC) provided illumination for the eye tracking channel (orange path), composed by a wide-field pupil imaging system using a CMOS camera with enhanced sensitivity in the near infrared (UI-1240LE-NIR-GL, Imaging Development Systems GmbH, Germany). The three channels were combined by means of two dichroic mirrors, DM1 (#39-656, Edmund Optics Inc., USA) and DM2 (FM03R, Thorlabs Inc., USA).

The OCT channel of the sample arm consisted in a dual path configuration. A fold mirror (FM) allowed switching from the anterior segment (red) to the posterior segment (pink) imaging mode.

The anterior segment interface (red) consisted of a fiber collimator C1, the set of galvanometric mirrors, mirrors M1-M3 and three groups of lenses: L1, L2 and the objective lens, OC. The retinal interface shared the collimator C1, L1 and OC with the anterior segment one. Figure 2 shows separately the optical designs of the anterior segment and retina imaging interfaces. The design and optimization of the optical interface was carried out in Zemax (Radiant Zemax LLC, USA). The Liou-Brennan eye model was used in the simulations of the retinal imaging modality performance [24].

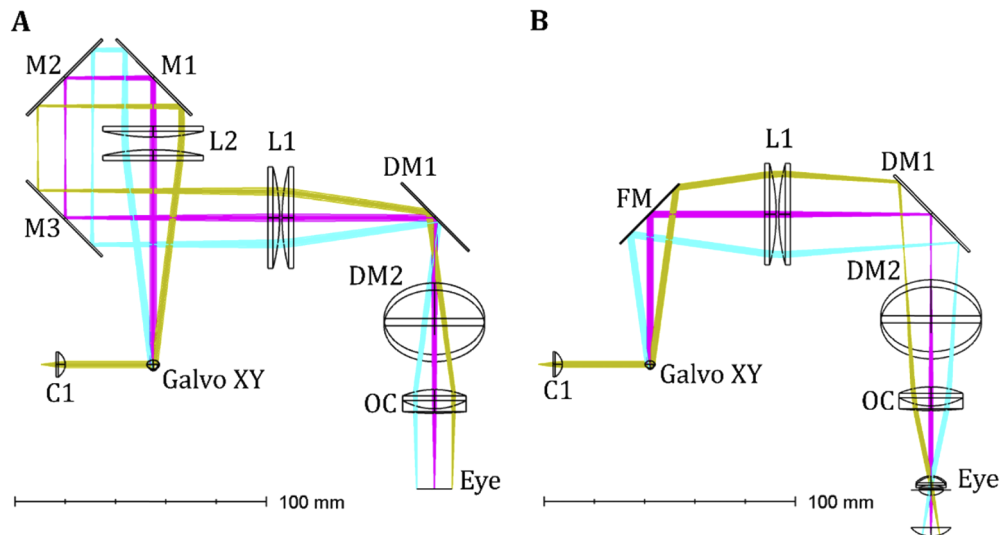


Fig. 2. Optical design of the sample arm: (A) anterior segment imaging modality, (B) retinal imaging modality (same notation for elements is used).

The group of lenses L1 and L2 were composed by pairs of singlets of diameter 40 mm and focal lengths of 150 mm and 170 mm (SLB-40-150PIR2 and SLB-40-170PIR2, OptoSigma Europe SAS, France) respectively, featuring effective focal lengths of 77.3 mm and 88.3 mm, respectively. The objective lens was a commercial achromatic doublet with focal 50.2 mm and 25.4 mm diameter (AC254-50B-ML, Thorlabs Inc., USA).

The working distance of the system was 29.8 mm. The anterior segment design exhibited a telecentric configuration with the focus at the pupil plane with diffraction-limited performance (Airy disc radius of 32.5 μm) in a 14 mm \times 14 mm FOV, as it can be observed in Fig. 3(A). Inputting the beam size after the collimator, the simulation yielded a waist of the beam at the image plane for the central scanning position of 26.2 μm , with a Rayleigh range of 2.05 mm (depth of focus of 4.10 mm).

The retinal interface achieved diffraction-limited performance (Airy radius of 15.2 μm) over a circular FOV of 24° with respect to the nodal point of the eye model (Fig. 3(B)). The scanning pivot relayed approximately at the pupil plane. The simulated Gaussian beam spot at the retina was 11.5 μm and the Rayleigh range yielded 0.52 mm (depth of focus 1.04 mm).

Summarizing, the proposed design satisfied the requirements stated at the beginning of this section since it permitted to image both the anterior segment and the retina with good quality throughout the specified FOVs. The sample arm featured a simple configuration with only one nodal point for integration of the anterior and the retinal interfaces.

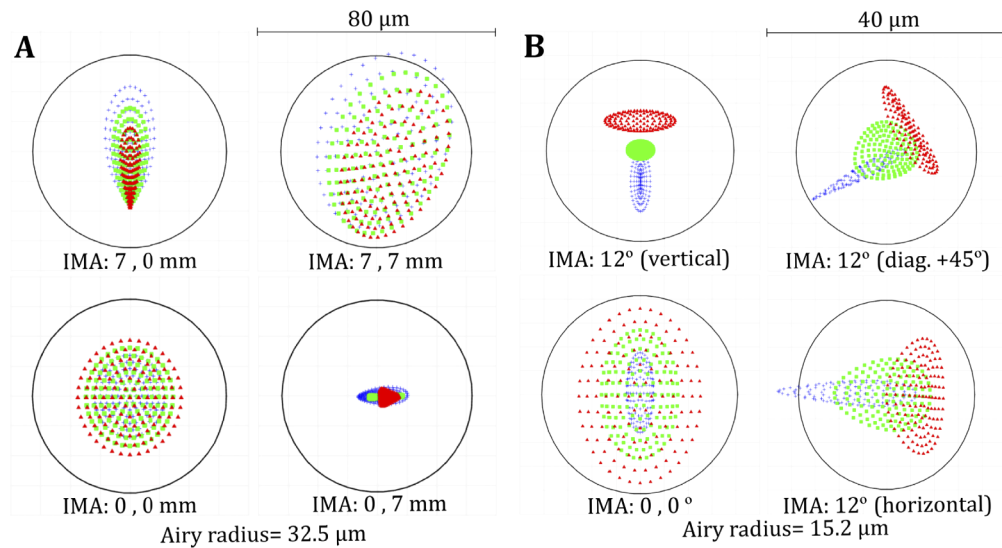


Fig. 3. Spot diagrams for on-axis, full horizontal, full vertical and diagonal FOVs in the (A) anterior segment and (B) retinal interfaces for three wavelengths: 1000 nm (blue), 1050 nm (green) and 1100 nm (red). The optical design can be considered to be diffraction-limited.

3. Results

A laboratory prototype was constructed as a proof of concept of the design described in the previous section. Commercial optomechanical parts were employed. The system performance was evaluated and the prototype was used to image a pilot population. A picture of the sample arm is depicted in Fig. 4.

3.1. Experimental characterization of the system

The experimental verification of the system specifications was assessed. First of all, the sensitivity roll-off of the system was measured.

For the anterior segment mode, acquisitions were taken at a fixed rate of 0.8 GS/s with 8192 samples per sweep. Post-processing steps were applied to the A-scans, including background subtraction, resampling for linearization in k -number domain and windowing of the spectrum using a Gaussian window (shaping). The resulting roll-off is shown in Fig. 5(A) in color curves. The peak sensitivity was 98 dB (at 1.8 mW laser power on the sample), while a roll-off of -6dB was reached at a depth of about 12 mm. The corresponding axial resolution, from Gaussian fits of the axial point spread functions, is also shown and corresponds to approximately 10 μm . The profile of the central beam in the anterior segment modality was studied with an infrared-enhanced CMOS sensor, and the beam diameter was determined by fitting a Gaussian function to the measured beam profile. The working distance of the system was determined to be 29 mm. The spot size and depth of focus of the central beam were 26.1 μm and 4.1 mm, respectively, in accordance with the results yielded by the simulation. Once located the position of the focal plane, the reference arm length was set to an equal distance by making the position to be the zero frequency in the zero coherence revival window. The effective sensitivity roll-off, also taking into account the loss in fiber coupling of backscattered photons out of focus, when the focal plane coincides with the zero-path length difference ($d = 0$ mm), is plotted with crosses in Fig. 5(A). It can be observed that the effective sensitivity decays much faster with depth. Resolution and all optical distances are all given in air.

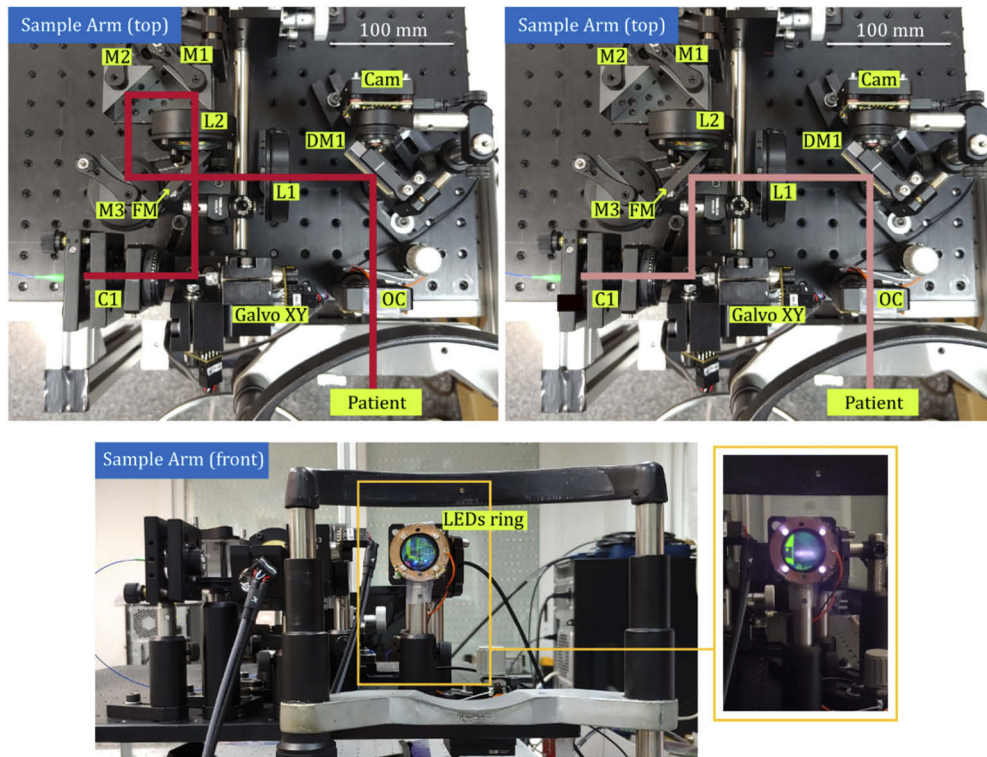


Fig. 4. Pictures of the laboratory prototype (top and front views) illustrating the implementation of the design of the sample arm (same notation for optical elements and optical path color identification as in Fig. 1). Detail of the LEDs ring switched on during laser scanning.

We studied the quality of anterior segment images for different values of the distance between the focal plane and the zero-delay plane, concluding that for a mismatch of $d = 6$ mm the visualization of the whole anterior segment structures was optimized [25]. The effective sensitivity in this condition is also shown with dots in Fig. 5(A). One can observe that the coherence length-related decay of sensitivity was compensated by the increasingly better efficiency in coupling when a mirror in the sample arm was displaced from the zero-path delay towards the focal plane.

In the retinal imaging mode, the k-clock signal generated by the swept source was employed to trigger signal sampling by the digitizer. The average frequency of the clock was about 250 MHz, providing a axial imaging range of 7.4 mm. Albeit too short for whole anterior segment imaging, this acquisition modality sufficed for retinal imaging. We characterized the sensitivity roll-off for this modality, which is shown in Fig. 5(B). Less than 1 dB decay in sensitivity was observed within the 7.4 mm imaging range. The axial resolution was about $11 \mu\text{m}$. The peak sensitivity was 104 dB at 1.8 mW of laser power on the sample. The difference in sensitivity between both interfaces might be caused by losses at the additional optics and mirrors in the anterior segment interface.

3.2. Eye safety

Eye safety compliance of the laser power was evaluated under the norm UNE-EN 60825-1. According to it, depending on the angle subtended at the cornea, a beam incident in the eye classifies as point-source (less than 1.5 mrad subtend) or extended source (greater than 1.5 mrad). In the retinal imaging modality the system delivered a collimated beam to the eye that produced

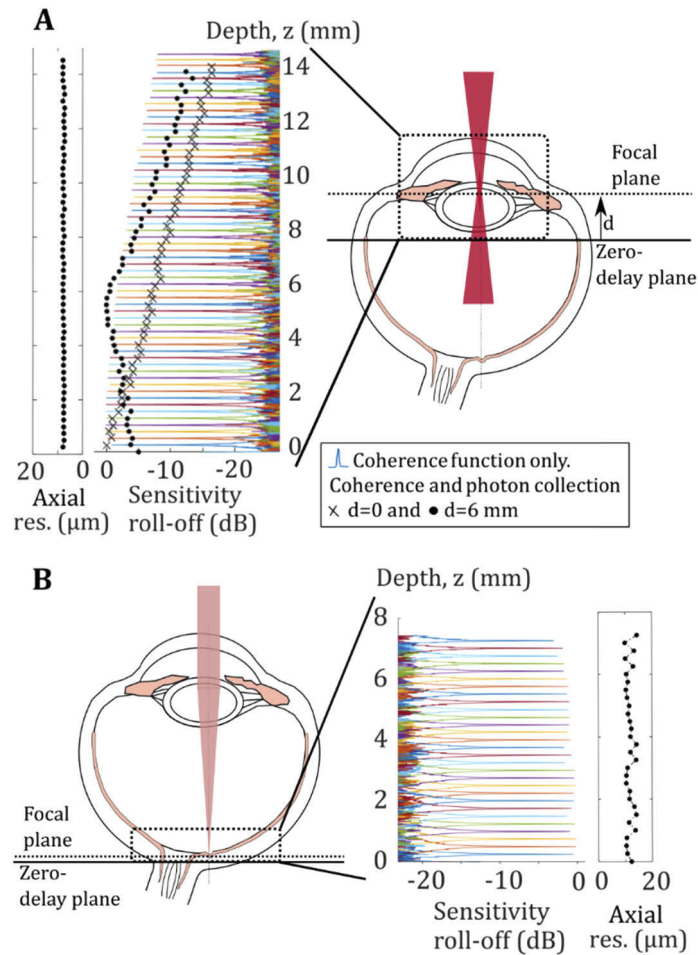


Fig. 5. Sensitivity roll-off and axial resolution of the anterior segment (A) and retinal (B) modes.

a small spot on the retina, and was thus considered as a point-source; whereas for the anterior segment modality a beam focusing approximately at the pupil plane of the eye was classified as an extended source.

The maximum permissible exposures (MPE) for 1050 nm, considering the conservative case of a static beam and exposure times of more than 25 s, were calculated to be 50 W/m^2 (point-source) and 1177.55 W/m^2 (extended source of corresponding subtense). The corresponding maximum permissible powers for ocular exposure were calculated as entering a pupil of 7 mm in diameter (0.385 cm^2), resulting in 1.95 mW (point-source) and 45.8 mW (extended source). The maximum optical power of the OCT signal at 1050 nm was measured to be 1.8 mW in either imaging modality. The applied power is then below the limits established by the norm for both the anterior and the retinal modality and therefore, the OCT instrument is safe for the human eye in both retinal and anterior segment imaging modalities.

We also evaluated the impact of the LEDs ring power in eye safety considerations according to the norm ISO 15004-2:2007. Following the measurement procedure indicated in it, the corresponding irradiance values for the cornea ($E_{\text{IR-CL}}$) and retina ($E_{\text{VIR-R}}$) of the 4 LEDs were $353.2 \mu\text{W/cm}^2$ and $121.5 \mu\text{W/cm}^2$, respectively. The limits for those irradiances for considering

the device as Group 1 are 20 mW/cm^2 ($E_{\text{IR-CL}}$) and 0.7 W/cm^2 ($E_{\text{VIR-R}}$), orders of magnitude above the values measured in our system. Therefore, the power delivered by the LED ring is safe for the human eye.

3.3. *In vivo imaging*

The prototype was deployed to the Institute of Ocular Microsurgery (Barcelona, Spain) to demonstrate the use of the proof of concept prototype as a whole eye OCT screening platform. Two groups were imaged: a small group of healthy volunteers and a small group of patients with anterior segment alterations, mainly corneal and/or lenticular opacifications. In the latter case, the eyes of the subjects were dilated. Each subject provided informed consent prior to any imaging under a protocol approved by the Ethical Committee at Institute of Ocular Microsurgery (Barcelona, Spain) and all measurements were performed according to the tenets of the declaration of Helsinki.

Volunteers were seated and stabilized on a standard chin rest while asked to fixate on a target. The system was aligned with respect to the subject's eye by means of the pupil camera, which was available during both retinal and anterior segment imaging. Real time display of OCT images permitted fine alignment. Anterior segment and retinal OCT measurements were acquired in a sequence with two different scan densities ($500 \text{ A-scans} \times 500 \text{ B-scans}$ and $2000 \text{ A-scans} \times 100 \text{ B-scans}$ for either modality). Manual actuation of the translation stages at the sample and the reference arm permitted to switch modalities and took about 4 seconds. If the second eye was to be measured too, the same protocol was repeated. Taking into account the time for alignment of both eyes, acquisitions recording itself, actuation and data storage, a measurement session took typically 10 minutes per subject.

Figure 6 shows OCT scans of a healthy volunteer (30 yo, female) imaged with the anterior segment and retinal modalities. The anterior segment images range from the corneal apex to the posterior face of the crystalline lens, permitting angle-to-angle visualizations, while the retinal images permit to resolve the main layers of the retina and permit to explore the optic disc and the macular region.

A healthy volunteer (35 yo, male) presented fully developed drusen-like deposits at the retinal pigment epithelium (RPE) level in the macular region as shown with the retinal modality (Fig. 7). The volunteer did not report any visual symptoms and scores 20/20 in visual acuity tests. As a consequence of the exam, the volunteer was referred to a retina specialist.

Anterior segment images of a volunteer (48 yo, female) who reported a sudden loss in vision quality in the right eye are shown in Fig. 8. A cataract specialist diagnosed her by means of a slit lamp biomicroscope exam with posterior subcapsular cataract with degree 3 in the right eye, according to the Lens Opacification Classification System III (LOCS III). OCT images confirmed increased backscattering originating from the posterior capsule of the lens in the right eye, but also morphological changes in the anterior capsule can be appreciated in the OCT images (Fig. 8(A)). The patient had perfect visual acuity in the left eye and no findings were reported under exploration. However, whole anterior segment OCT acquisitions permitted to identify morphological changes in the crystalline lens in the form of micro-opacifications in the periphery of the cortex (Fig. 8(B, C)), which could be an indicator of lenticular degeneration and precede more drastic changes in the structure of the lens [25].

Figure 9 shows the anterior segment images of a volunteer (46 yo, male) who experienced a gradual decrease in visual quality. A cataract specialist diagnosed him by means of a slit lamp exam with posterior subcapsular cataract with degree 2 in both eyes. OCT captures with the prototype permitted to locate the lesion within the lens with better accuracy, showing that rather than in the posterior lens capsule, the cataract lesion was located in the posterior cortex (Fig. 9(A)). Additionally, micro-opacifications can also be observed, describing a spoke-like distribution in the lens (Fig. 9(B)).

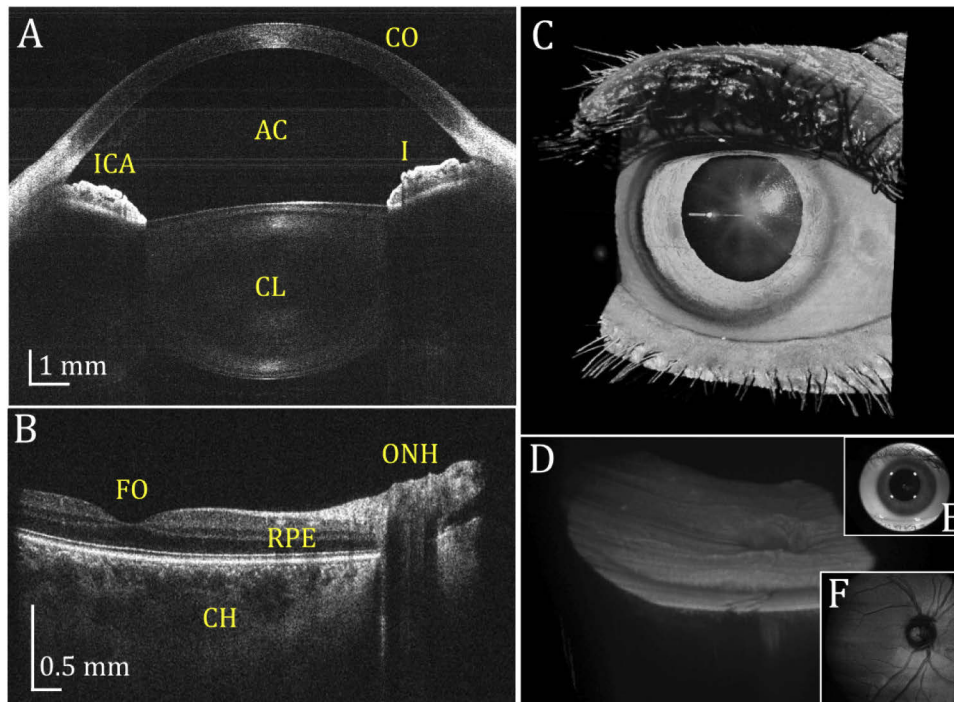


Fig. 6. Healthy volunteer imaged with the prototype. Single unaveraged OCT images (2000 A-scans/B-scan) with the anterior segment (A) and retinal (B) imaging modalities. Volume rendering of 3-D OCT data sets (500 A-scans \times 500 B-scans) of the anterior segment (C) and the retina (D). Frame acquired during alignment on the pupil camera (E) and *en-face* visualization of the retinal volumetric data (F). CO – cornea, AC – anterior chamber, I – iris, ICA – iridocorneal angle, CL – crystalline lens, RPE – retinal pigment epithelium, ONH – optic nerve head (optic disc), CH – choroid.

As the whole anterior segment was imaged, the visualization of clinically relevant details in the cornea, crystalline lens, iris and iridocorneal angle on single-shot acquired images was possible. Figure 10 shows B-scans and volume renderings of two volunteers presenting opacifications in the cornea and in the lens. A central B-scan of a volunteer (57 yo, female) in Fig. 10(A) shows a central corneal opacification (leukoma), growth of tissue causing adherences of the iris to the lens (synechias) and increased backscattering from the nucleus of the lens, suggesting a nuclear cataract. Moreover, the volume rendering of the same patient permits to observe the abnormal shape of the pupil and corneal neovascularization (Fig. 10(B)). Figure 10(C) presents the OCT B-scan and volume rendering of a volunteer (77 yo, female) with corneal scars and anterior and posterior cortical cataract. The volume rendering allowed to determine the location and extent of the corneal scars (Fig. 10(D)) and the sutures of the lens could be appreciated, as well [26].

Additionally, whole anterior segment B-scans also permitted to evaluate the iridocorneal angle. The patient shown in Fig. 10(A) exhibits extremely closed iridocorneal angle and a narrow anterior chamber depth, which are known as risk factors for the development of close-angle glaucoma. On the contrary, the patient shown in Fig. 10(B) has an ample chamber with wide open iridocorneal angles. The enhanced depth imaging range of the developed anterior segment modality also permitted to image the interface between the lens and the vitreous. An example of this can be found in Fig. 10(E), where we show the volume rendering of a volunteer (8 yo, male) who exhibited a large vitreal structure in contact with the posterior part of the lens, where

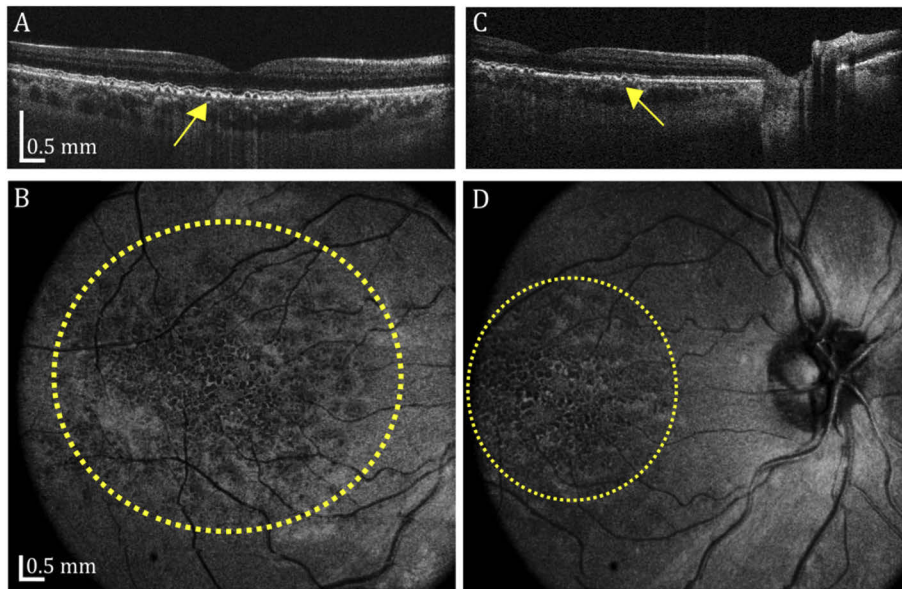


Fig. 7. Asymptomatic volunteer (35 yo, male) presented drusen-like deposits at the RPE level as shown in the retinal captures. OCT acquisitions were taken centered at the fovea (A, B) and also including the optic disc (C, D). B-scans with 2000 A-scans (top). *En-face* reconstructions optimized for visualization of lesions at RPE from 500 A-scans \times 500 B-scans data sets (bottom) showed the area under the macula was affected by the presence of drusen.

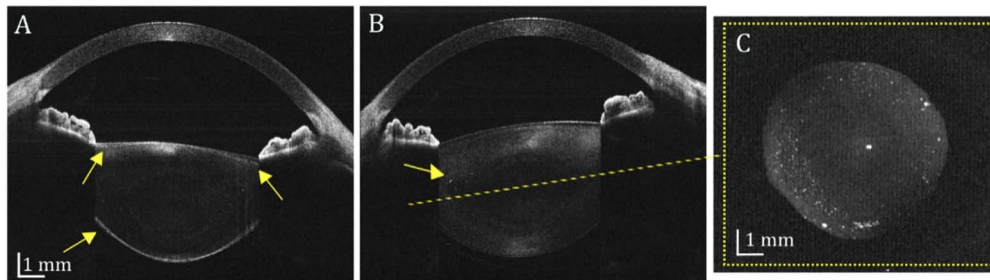


Fig. 8. Volunteer (48 yo, female) who reported a sudden loss of vision in the right eye shows morphological changes in the lens localized in the posterior and anterior capsule (A). The patient did not report changes in her visual perception in the left eye and no findings were reported during medical exploration, but OCT scans reveals micro-opacifications in the peripheral cortex in B-scans (B) and *en-face* images. (C).

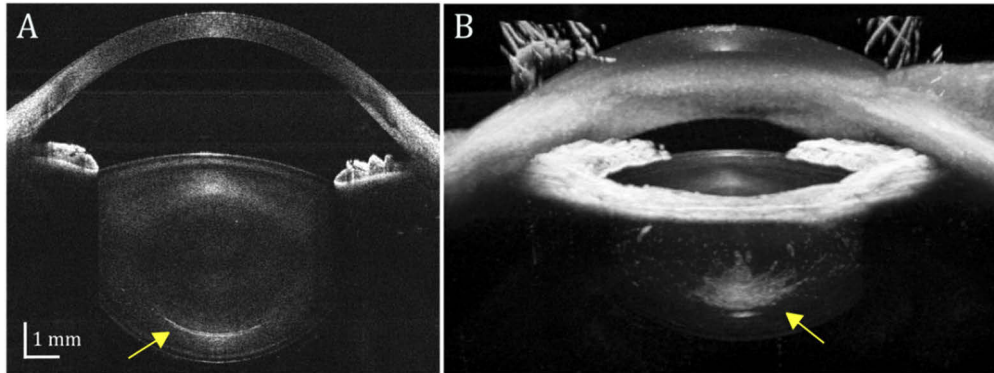


Fig. 9. Volunteer (46 yo, male) who reported a gradual decrease in visual acuity exhibited a cataract-like lesion in the posterior cortex of the crystalline lens as it can be observed in central B-scan with 2000 A-scans (A). Volume rendering from 500 A-scans \times 500 B-scans measurement (B) permitted to visualize cortical micro-opacifications in a spoke-like distribution.

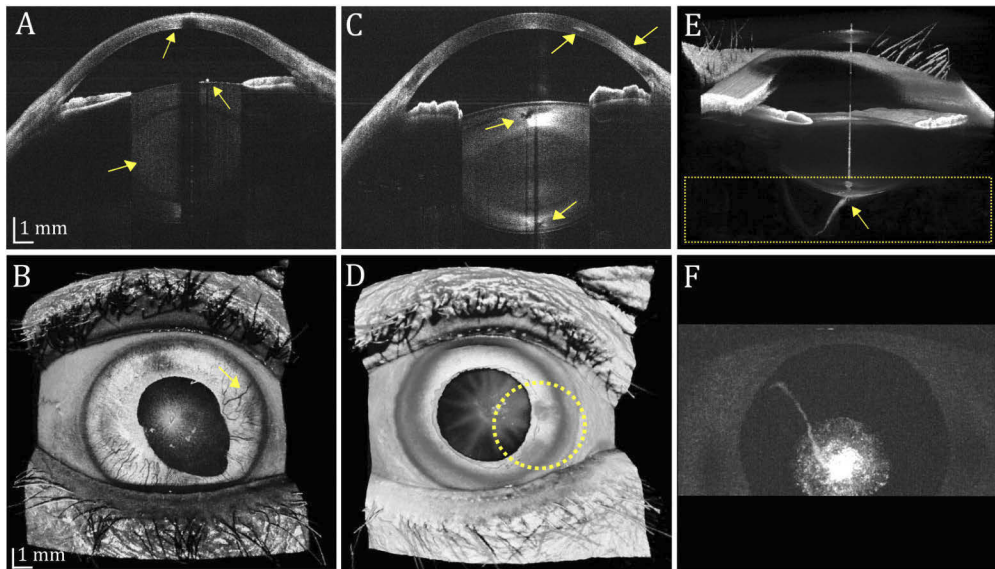


Fig. 10. Whole anterior segment OCT images permitted to evaluate clinically relevant features at different depths in captures acquired in a single shot. (A, B) Volunteer (57 yo, female) presented a central corneal leukoma, synechias causing pupillary dyscoria, neovascularization and nuclear cataract. (C, D) Volunteer (77 yo, female) showed mature cataract lesions at the anterior and posterior cortex of the lens and also corneal scars. (E, F) Volunteer (8 yo, male) exhibited a large vitreal structure in contact with the posterior part of the lens, where a cataract lesion was observed. The sum intensity projection in F comes from the slab indicated by a dashed line.

a cataract lesion was observed. Access to volumetric data allowed to select a region (3 mm-thick slab) to generate an *en-face* projection image. Sum intensity projection, generated by axial summation of the OCT signal from the slab, showed additional information regarding the extent of the cataract lesion (Fig. 10(F)).

4. Discussion and conclusion

We have demonstrated a whole anterior segment and retinal SS-OCT system. The clinical use of the proof of concept system for whole eye visualizations in a pilot population, including healthy and pathological subjects, has been presented. The results showed its utility in the description of clinical findings in the retina and the anterior segment of both symptomatic and asymptomatic volunteers.

The system combines the well-known clinical capabilities of conventional retinal OCT with entire anterior segment OCT imaging, which provides a powerful platform for diagnostics of anterior segment alterations. We have shown clinical examples of eye morphology alterations revealed by SS-OCT imaging in patients who did not have any visual symptoms. We have also provided examples where whole anterior OCT images permitted to improve the accuracy of a diagnosis or permitted the visualization of clinical findings that were not identified under usual ophthalmologic exploration.

Additionally, the system has the potential of generating complete biometric information of the eye, provided that the images are properly corrected for optical system distortions and for light refraction caused by optical properties of the patient's eye. Thanks to whole eye visualization, including the whole lens, a fully personalized distortion correction of the data sets can be carried out [27,28].

Whole eye morphological and biometric information in one platform could be valuable in the diagnosis, follow-up and treatment of a number of ocular pathologies that affect both segments of the eye. For example, during the assessment of glaucoma, specialists usually evaluate the thinning of specific layers in the macular and optic disc regions in retinal OCT scans but also assess the iridocorneal angles [8]. Indeed, not only do these measurements aid in the diagnosis of glaucoma, but they also often serve as a clinical basis to take preventive measures against the development of the disease, such as laser iridotomies.

Whole eye OCT could also be of value in the management of cataract. It has been shown that OCT images of the entire anterior segment can help evaluate three-dimensional microstructural changes of the lens [25,29,30], which in turn could provide additional information for the diagnosis and grading of different types of cataracts. A whole eye OCT platform could also provide the biometric information required for cataract surgery planning, which usually includes a pre-surgery retinal OCT exam for screening. One of the major complications in cataract surgery is posterior capsule rupture during phacoemulsification. It has been demonstrated that OCT images showing the whole anterior segment, including the posterior part of the lens, provide insight into posterior capsule integrity preoperatively [31]. Whole eye OCT is also useful in the post-surgical evaluation of the positioning of the implanted lens [32]. Specifically, when capsule/zonular support for the intraocular lens is not available, less conventional surgical approaches are employed, during which centering and positioning of the lens can be challenging. A whole eye OCT platform could provide relevant information for evaluation and investigation of different surgical techniques in those challenging conditions [33,34]. In addition, lenticular opacities affect transparency of the lens and influence the light levels reaching the retina. Consequently, retinal imaging could suffer from the opacification of the crystalline lens. The imaging tool presented in this study could be used to investigate the relation between cataract severity and retinal image quality (and extracted retinal biomarkers) [35–37]. Commercially available OCT systems that image the retina and the anterior segment do not typically image the whole anterior segment, therefore presenting

limitations in the above mentioned clinical applications, which require imaging of the entire crystalline lens.

In our whole eye OCT design, we have opted for a sequential retinal – anterior segment configuration, in contrast to simultaneous configurations which offer the benefit of acquiring the whole eye data set in a single shot. As a disadvantage, those platforms need to limit the amount of laser power that is sent to each segment of the eye, so that joint exposure does not exceed the limits indicated by eye safety considerations, which might decrease the quality of the images. Moreover, in systems based on polarization multiplexing, backscattered photons that do not match the input polarization mode of the system are sent to the orthogonal mode. If properly designed, they will not contribute to the noise in the other channel, being rejected by the coherence gate. Nevertheless, they cause the signal-to-noise ratio (SNR) to drop below the measured sensitivity of the system, meaning that the sensitivity of the system will depend on the birefringence of the tissues under examination, too. The solution presented in this work utilizes only one node for the integration of the anterior segment and retinal modalities, reducing its complexity. If desired, a polarization multiplexing simultaneous configuration could be also easily adapted by using a polarization splitting element instead of the fold mirror.

An important limitation of the current experimental implementation of the system is the manual actuation of two translation stages in both the reference and sample arm to switch for anterior to retinal imaging. The use of motorized linear stages to insert the fold mirror in the sample arm and to adapt the length of the reference arm could greatly ease the use of such a system in a clinical environment. Alternatively, the reference arm could be used at a fixed length, so that the zero coherence revival window is used for imaging of the whole anterior segment and the retina is imaged in a successive coherence window.

Improvements of the system could also include the design of a wider field of view in the retinal modality but still capable of imaging the whole anterior segment. A recent wide field of view whole eye OCT system has stimulated interesting clinical applications exploiting the estimation of retinal curvature [18]. This platform, however, only imaged the anterior chamber. While it is argued that for the extraction of quantitative retinal curvature estimation whole anterior segment biometry is not crucial, a number of biometric applications would profit from combined whole anterior segment and retinal curvature data, such as ocular developmental studies.

Another aspect of the prototype that could be revised is the speed rate of the source. Short cavity swept lasers come with a trade off in coherence length and sweep rate. In our case, a 50 kHz laser source was selected to offer a coherence length enough for whole anterior segment imaging. Currently, there are swept sources of a higher sweep rate that could provide sufficiently long coherence length [23]. A faster scanning source could decrease the incidence of ocular movements during the measurement.

We also would like to point out that the optical design of the sample arm of the system is compatible for integration into a system for evaluation of the visual function based on eye tracked tasks developed in a previous work [38]. One of the prospects of the work presented here is the combination of whole eye OCT images and eye tracking registers in the characterization of the visual function of a patient, since recent works have shown that eye tracked experiments could reproduce in a more repeatable and objective manner traditional optometric tests [39]. These tests are used for the evaluation of oculomotor dysfunctions, which usually include the subjective interpretation of the clinician and are affected by how collaborative the patient is. Such a combined system could provide not only OCT data sets of the whole eye, but also oculomotor information, collecting comprehensive information about the patient visual health. This could be of use in the study of the relation between morphological and oculomotor biomarkers in certain pathologies [40–42]. We also envision that whole eye OCT data sets, and eventually combined with eye tracking registers, could be exploited by advanced analytic techniques in the development of powerful computer aided diagnosis of ocular pathologies.

In conclusion, we have developed a dual path SS-OCT system capable of imaging the whole anterior segment and the retina in a sequence. We have demonstrated the clinical potential of the prototype for whole eye screening and early detection of morphological changes both in the anterior segment and the retina.

Funding. European Union's Research and Innovation Program (675512, BE-OPTICAL); Foundation for Polish Science (POIR.04.04.00-00-5C9B/17-00 TEAM).

Acknowledgment. The authors would like to thank the ophthalmologists, as well as the clinical trials and ocular photography departments at IMO for their help with the measurements and clinical feedback. The authors would also like to thank the volunteers that have participated in the clinical study.

Disclosures. The authors declare that there are no conflicts of interest related to this article.

References

1. D. Huang, E. A. Swanson, C. P. Lin, J. S. Schuman, W. G. Stinson, W. Chang, M. R. Hee, T. Flotte, K. Gregory, C. A. Puliafito, and J. G. Fujimoto, "Optical coherence tomography," *Science* **254**(5035), 1178–1181 (1991).
2. C. K. Hitzenberger, W. Drexler, R. A. Leitgeb, O. Findl, and A. F. Fercher, "Key Developments for Partial Coherence Biometry and Optical Coherence Tomography in the Human Eye Made in Vienna," *Invest. Ophthalmol. Visual Sci.* **57**(9), OCT460–OCT474 (2016).
3. E. A. Swanson, J. A. Izatt, M. R. Hee, D. Huang, C. P. Lin, J. S. Schuman, C. A. Puliafito, and J. G. Fujimoto, "In vivo retinal imaging by optical coherence tomography," *Opt. Lett.* **18**(21), 1864–1866 (1993).
4. J. A. Izatt, M. R. Hee, E. A. Swanson, C. P. Lin, D. Huang, J. S. Schuman, C. A. Puliafito, and J. G. Fujimoto, "Micrometer- scale resolution imaging of the anterior eye in vivo with optical coherence tomography," *Arch. Ophthalmol.* **112**(12), 1584–1589 (1994).
5. M. Wojtkowski, R. Leitgeb, A. Kowalczyk, T. Bajraszewski, and A. F. Fercher, "In vivo human retinal imaging by Fourier domain optical coherence tomography," *J. Biomed. Opt.* **7**(3), 457–463 (2002).
6. B. Bouma and G. Tearney, eds., *Handbook of Optical Coherence Tomography* (Marcel-Dekker, 2002).
7. W. Drexler and J. G. Fujimoto, eds., *Optical Coherence Tomography* (Springer-Verlag, 2008).
8. I. Grulkowski, "Anterior segment OCT," in *Handbook of Visual Optics, Volume Two: Instrumentation and Vision*, P. Artal, ed. CRC Press - Taylor & Francis Group (2016).
9. A. N. Kuo, R. McNabb, and J. A. Izatt, "Advances in Whole-Eye Optical Coherence Tomography Imaging," *Asia-Pac. J. Ophthalmol.* **8**(2), 99–104 (2019).
10. M. Ruggieri, S. R. Uhlhorn, C. De Freitas, A. Ho, F. Manns, and J.-M. Parel, "Imaging and full-length biometry of the eye during accommodation using spectral domain OCT with an optical switch," *Biomed. Opt. Express* **3**(7), 1506–1520 (2012).
11. H.-W. Jeong, S.-W. Lee, and B.-M. Kim, "Spectral-domain OCT with dual illumination and interlaced detection for simultaneous anterior segment and retina imaging," *Opt. Express* **20**(17), 19148–19159 (2012).
12. C. Dai, C. Zhou, S. Fan, Z. Chen, X. Chai, Q. Ren, and S. Jiao, "Optical coherence tomography for whole eye segment imaging," *Opt. Express* **20**(6), 6109–6115 (2012).
13. S. Fan, L. Li, C. Dai, Q. Ren, S. Jiao, and C. Zhou, "Dual band dual focus optical coherence tomography for imaging the whole eye segment," *Biomed. Opt. Express* **6**(7), 2481–2493 (2015).
14. I. Grulkowski, J. J. Liu, B. Potsaid, V. Jayaraman, C. D. Lu, J. Jiang, A. E. Cable, J. S. Duker, and J. G. Fujimoto, "Retinal, anterior segment and full eye imaging using ultrahigh speed swept source OCT with vertical cavity surface emitting lasers," *Biomed. Opt. Express* **3**(11), 2733–2751 (2012).
15. I. Grulkowski, S. Manzanera, L. Cwiklinski, F. Sobczuk, K. Karnowski, and P. Artal, "Swept source optical coherence tomography and tunable lens technology for comprehensive imaging and biometry of the whole eye," *Optica* **5**(1), 52–59 (2018).
16. A.-H. Dhalla, D. Nankivil, and J. A. Izatt, "Complex conjugate resolved heterodyne swept source optical coherence tomography using coherence revival," *Biomed. Opt. Express* **3**(3), 633–649 (2012).
17. A.-H. Dhalla, D. Nankivil, T. Bustamante, A. Kuo, and J. A. Izatt, "Simultaneous swept source optical coherence tomography of the anterior segment and retina using coherence revival," *Opt. Lett.* **37**(11), 1883–1885 (2012).
18. D. Nankivil, G. Waterman, F. LaRocca, B. Keller, A. N. Kuo, and J. A. Izatt, "Handheld, rapidly switchable, anterior/posterior segment swept source optical coherence tomography probe," *Biomed. Opt. Express* **6**(11), 4516–4528 (2015).
19. R. P. McNabb, J. Polans, B. Keller, M. Jackson-Atogi, C. L. James, R. R. Vann, J. A. Izatt, and A. M. Kuo, "Wide-field whole eye OCT system with demonstration of quantitative retinal curvature estimation," *Biomed. Opt. Express* **10**(1), 338–355 (2019).
20. H. J. Kim, M. Kim, M. G. Hyeon, Y. Choi, and B. M. Kim, "Full ocular biometry through dual-depth whole-eye optical coherence tomography," *Biomed. Opt. Express* **9**(2), 360–372 (2018).
21. R. Chopra, P. J. Mulholland, A. M. Dubis, R. S. Anderson, and P. A. Keane, "Human Factor and Usability Testing of a Binocular Optical Coherence Tomography System," *Trans. Vis. Sci. Tech.* **6**(4), 16 (2017).
22. R. Chopra, P. J. Mulholland, V. K. Tailor, R. S. Anderson, and P. A. Keane, "Use of a Binocular Optical Coherence Tomography System to Evaluate Strabismus in Primary Position," *JAMA Ophthalmol.* **136**(7), 811–817 (2018).

23. T. Klein and R. Huber, "High-speed OCT light sources and systems [Invited]," *Biomed. Opt. Express* **8**(2), 828–859 (2017).
24. H.-L. Liou and N. A. Brennan, "Anatomically accurate, finite model eye for optical modeling," *J. Opt. Soc. Am. A* **14**(8), 1684–1695 (1997).
25. I. Grulkowski, S. Manzanera, L. Cwiklinski, J. Mompeán, A. de Castro, J. M. Marin, and P. Artal, "Volumetric macro- and micro-scale assessment of crystalline lens opacities in cataract patients using long-depth-range swept source optical coherence tomography," *Biomed. Opt. Express* **9**(8), 3821–3833 (2018).
26. A. Gupta, D. Ruminski, A. Jimenez Villar, R. Duarte Toledo, S. Manzanera, S. Panezai, J. Mompean, P. Artal, and I. Grulkowski, "In vivo SS-OCT imaging of crystalline lens sutures," *Biomed. Opt. Express* **11**(10), 5388–5400 (2020).
27. S. Ortiz, D. Siedlecki, I. Grulkowski, L. Remon, D. Pascual, M. Wojtkowski, and S. Marcos, "Optical distortion correction in optical coherence tomography for quantitative ocular anterior segment by three-dimensional imaging," *Opt. Express* **18**(3), 2782–2796 (2010).
28. D. Siedlecki, A. De Castro, E. Gamba, S. Ortiz, D. Borja, S. Uhlhorn, F. Manns, S. Marcos, and J.-M. Parel, "Distortion correction of OCT images of the crystalline lens: Gradient index approach," *Optometry and Vision Science* **89**(5), E709–E718 (2012).
29. A. de Castro, A. Benito, S. Manzanera, J. Mompeán, B. Cañizares, D. Martínez, J. M. Marín, I. Grulkowski, and P. Artal, "Three-dimensional cataract crystalline lens imaging with swept-source optical coherence tomography," *Invest. Ophthalmol. Visual Sci.* **59**(2), 897–903 (2018).
30. P. Eugui, D. J. Harper, S. Kummer, A. Lichtenegger, J. Gesperger, T. Himmel, M. Augustin, C. W. Merkle, M. Glösmann, and B. Baumann, "Three-dimensional visualization of opacifications in the murine crystalline lens by in vivo optical coherence tomography," *Biomed. Opt. Express* **11**(4), 2085–2097 (2020).
31. A. Pujari, S. Yadav, N. Sharma, S. Khokhar, R. Sinha, T. Agarwal, J. S. Titiyal, and P. Sharma, "Study 1: Evaluation of the signs of deficient posterior capsule in posterior polar cataracts using anterior segment optical coherence tomography," *J. Cataract Refractive Surg.* **46**(9), 1260–1265 (2020).
32. E. Martínez-Enríquez, P. Pérez-Merino, S. Durán-Poveda, I. Jiménez-Alfaro, and S. Marcos, "Estimation of intraocular lens position from full crystalline lens geometry: towards a new generation of intraocular lens power calculation formulas," *Sci. Rep.* **8**(1), 9829 (2018).
33. K. Hayashi, A. Hirata, and H. Hayashi, "In-the-bag scleral suturing of intraocular lens in eyes with severe zonular dehiscence," *Eye* **26**(1), 88–95 (2012).
34. S. Ni, W. Wang, X. Chen, X. Wu, S. He, Y. Ma, and W. Xu, "Clinical observation of a novel technique: transscleral suture fixation of a foldable 3-looped haptics one-piece posterior chamber intraocular lens implantation through scleral pockets with intact conjunctiva," *BMC Ophthalmol.* **19**(1), 105 (2019).
35. M. E. van Velthoven, M. H. van der Linden, M. D. de Smet, D. J. Faber, and F. D. Verbraak, "Influence of cataract on optical coherence tomography image quality and retinal thickness" [published correction appears in *Br J Ophthalmol.* 2010 Dec;94(12):1695], *Br. J. Ophthalmol.* **90**(10), 1259–1262 (2006).
36. M. Kim, Y. Eom, J. S. Song, and H. M. Kim, "Effect of Cataract Grade according to Wide-Field Fundus Images on Measurement of Macular Thickness in Cataract Patients," *Korean J. Ophthalmol.* **32**(3), 172–181 (2018).
37. S. Yu, B. E. Frueh, D. Steinmair, A. Ebnetter, S. Wolf, M. S. Zinkernagel, and M. R. Munk, "Cataract significantly influences quantitative measurements on swept-source optical coherence tomography angiography imaging," *PLoS One* **13**(10), e0204501 (2018).
38. C. Mestre, J. Gautier, and J. Pujol, "Robust eye tracking based on multiple corneal reflections for clinical applications," *J. Biomed. Opt.* **23**(03), 1 (2018).
39. C. Mestre, C. Otero, F. Díaz-Doutón, J. Gautier, and J. Pujol, "An automated and objective cover test to measure heterophoria," *PLoS One* **13**(11), e0206674 (2018).
40. T. Anderson and M. MacAskill, "Eye movements in patients with neurodegenerative disorders," *Nat. Rev. Neurol.* **9**(2), 74–85 (2013).
41. C. Antoniadis and C. Kennard, "Ocular motor abnormalities in neurodegenerative disorders," *Eye* **29**(2), 200–207 (2015).
42. M. Bartuzel, K. Wróbel, S. Tamborski, M. Meina, M. Nowakowski, K. Dalasiński, A. Szkulmowska, and M. Szkulmowski, "High-resolution, ultrafast, wide-field retinal eye-tracking for enhanced quantification of fixational and saccadic motion," *Biomed. Opt. Express* **11**(6), 3164–3180 (2020).